



Implicit Shape Modeling for Anatomical Structure Refinement of Volumetric Medical Images

Minghui Zhang^{a,b,c}, Hanxiao Zhang^a, Xin You^{a,b,c}, Guang-Zhong Yang^a, Yun Gu^{a,b,c,*}

^aInstitute of Medical Robotics, Shanghai Jiao Tong University, Shanghai, 200240, China

^bInstitute of Image Processing and Pattern Recognition, Shanghai Jiao Tong University, Shanghai, 200240, China

^cDepartment of Automation, Shanghai Jiao Tong University, Shanghai, 200240, China

ARTICLE INFO

Article history:

2000 MSC: 41A05, 41A10, 65D05, 65D17

Keywords: Implicit Representation on Medical Shapes, Structure Refinement, Topological Prior Knowledge.

ABSTRACT

Shape modeling of volumetric data is essential for medical image analysis and computer-aided intervention. In practice, automated shape reconstruction cannot always achieve satisfactory results due to limited image resolution and a lack of sufficiently detailed shape priors used as constraints. In this paper, a unified framework is proposed for 3D shape modelling and segmentation refinement based on implicit neural networks. To learn a sharable shape prior from different instances within the same category during training, physical details of volumetric data are firstly used to construct Physical-Informed Continuous Coordinate Transform (PICCT) for implicit shape modeling. For improved shape representation, implicit shape constraints based on Signed Distance Function (SDF) are used for both instances and latent templates. For inference, a Template Interaction Module (TIM) is proposed to refine 3D shapes produced by Convolutional Neural Networks (CNNs) via deforming deep implicit templates with latent codes. Experimental results on validation datasets involving liver, pancreas and lung segmentation demonstrate the superiority of our approach in shape refinement and reconstruction. The Chamfer Distance/Earth Mover's Distance achieved by the proposed method are 0.232/0.087 for the Liver dataset, 0.128/0.069 for the Pancreas dataset, and 0.417/0.100 for the Lung Lobe dataset, respectively. The source code is available at: <https://github.com/EndoluminalSurgicalVision-IMR/ISMM>.

© 2024 Elsevier B. V. All rights reserved.

1. Introduction

3D Shape modeling of volumetric data is a pre-requisite to medical image analysis and computer-aided intervention (Pelani et al., 2020; Krass et al., 2022; Preuss et al., 2022). They are also used extensively in Augment Reality (AR) and Virtual Reality (VR) based surgical planning, allowing improved appreciation of complex anatomies involving critical structures

to be dissected or preserved (Edgcumbe et al., 2015; Ramalhinho et al., 2023; Huber et al., 2017; Willaert et al., 2012). In recent years, the use of deep learning models (Litjens et al., 2017), especially the U-Shape neural networks (UNet) (Ronneberger et al., 2015; Çiçek et al., 2016; Dou et al., 2017) have attracted extensive interests. UNet models are designed on top of CNNs with a skip connection between the encoder and decoder. Although the architecture exhibits great inductive capability, it is faced with several challenges in practical shape modeling in medical imaging analysis. First, 3D UNet (Çiçek et al., 2016) may generate structural errors due to a lack of shape priors as the constraint. Second, CNN-based methods are sus-

*Corresponding authors.

e-mail: geron762@sjtu.edu.cn (Yun Gu)

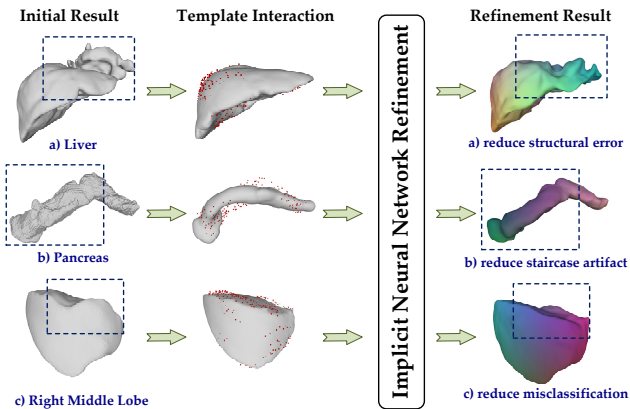


Fig. 1. The proposed method interacts with initial results with the corresponding implicit template via implicit neural networks to achieve refined results.

ceptible to low image resolution. They can only approximate organ contours as they are limited to the discrete voxel grid. Third, due to its excessive use of GPU memory, UNet models for 3D volumetric segmentation have to adopt a patch-wise training and testing paradigm, which affects the modelling of long-range dependency of anatomical structures. These difficulties can lead to structural errors (as seen in Fig.1.a), initial segmentation result of the liver structure by 3D UNet), staircase artifact of the boundary (as seen in Fig.1.b) initial result of the pancreas), and misclassification problems in the shape modeling (as seen in Fig.1.c) initial result of the right middle lobe). Previous work involved multi-stage refinement methods, e.g., cascaded UNet structures (Jha et al., 2020), adversarial structure correction (Dai et al., 2018), and variational auto encoder that improves topology coherence (Araújo et al., 2019), to refine the initial prediction results by CNNs. However, these extra refinement modules cannot generate explainable shape prior, leading to uncontrollable 3D shape results. In addition, these methods still relied on the discrete voxel grid and could not impose physically strong shape constraints. For this reason, the improvement achievable remains limited. Prior to deep learning era, Statistical Shape Models (SSMs) (Heimann and Meinzer, 2009) own better explainability because they impose plausible anatomical constraints on shapes. However, classical SSMs methods mainly rely on Point Distribution Model (PDM) (Cootes et al., 1992), which requires a well-defined correspondence across shapes. Further, the statistics of SSMs that based on level set representation were sampled across the 3D regular grid (Cremers et al., 2007), hindering the shape modeling in the continuous physical space.

To alleviate these drawbacks in shape modeling and refinement, as suggested in the explainable AI system (Gunning et al., 2019), our goal is to develop a unified framework to first learn the explainable within-class shape prior in the continuous physical space, the correspondence between the instance and learned shape prior is simultaneously built. The shape prior is then used as the explainable template to refine the 3D shapes, ensuring the refinement procedure controllable and interpretable. Recently, Implicit Neural Representation (INR) networks, which model continuous, differentiable signal repre-

sentations (Park et al., 2019; Chen and Zhang, 2019; Mescheder et al., 2019; Sitzmann et al., 2020; Peng et al., 2020; Sitzmann et al., 2019; Chabra et al., 2020; Jiang et al., 2020) have been used to break the limitation of the discrete voxel grid. INRs employ coordinate based neural networks to parameterize the physical properties of 3D objects or scenes. These methods have emerged as a powerful tool for 3D modelling in natural scenes but have not yet been used in medical imaging due to intrinsic differences of the two application scenarios.

This is because synthetic models for natural scenes (Chang et al., 2015) tend to be rigidly aligned and suited to shape reconstruction/completion tasks by INRs (Park et al., 2019; Chen and Zhang, 2019; Mescheder et al., 2019; Chibane et al., 2020). Medical images, however, can be acquired from different modalities with contrastingly different appearances. Compared to modern video cameras, the spatial resolution of medical imaging is relatively low and is often anisotropic. These conditions can lead to the spatial distribution of anatomical shapes under the world coordinate system is always non-uniform. When feeding coordinates of disordered shapes to INRs, they will generate the template shape manifesting with floating artifacts, as demonstrated in Fig.2.a). These inaccurate shape priors are harmful to the refinement procedure, leading to low reliability and explainability. To impose the implicit surface as physical anatomical constraints, we proposed Physical-Informed Continuous Coordinate Transform (PICCT), which first utilizes the meta information, i.e., direction, origin, and spacing of volumetric data, to transform the coordinates from the image coordinate system to the world coordinate system. Next, PICCT samples points of the world coordinate from each sample to calculate the corresponding rigid transformation that transforms their anatomical structure from arbitrary distribution to the canonical frame. The aligned results can be seen in Fig.2.b), and the floating artifacts are removed in the implicit template learning.

Further, given that medical shapes share similarities across different instances, we hypothesize that the anatomical structure of an instance can be represented by a sharable implicit template field, together with its deformation field. Hence, we propose implicit shape modeling with template generation. Specifically, the sampling points of aligned instances, along with the assigned paired latent codes with each instance are input to INRs. INRs first map the latent code-conditioned inputs to the latent template space, simultaneously generating deformation field for each case. The deformation field is then used for instance-wise shape reconstruction. Inspired by (Park et al., 2019; Gropp et al., 2020), we introduce the continuous signed distance function (SDF) as a constraint to facilitate the shape representation of both template and instances during the training procedure. Although the INRs show great capability of shape modeling in continuous space, the generalization ability is hard to guarantee. Reconstruction of unseen objects (Park et al., 2019; Chen and Zhang, 2019; Mescheder et al., 2019; Chibane et al., 2020) still needs to sample points from unseen objects to finetune the INRs and latent codes. The sampled points from natural 3D data inherently possess semantic information, whereas the volumetric medical images do not. This

difference hinders the capacity of INRs to implicitly model unseen medical data. To deal with this limitation, we propose the template interaction module (TIM) that interacts with initial segmentation results from CNNs with learned template shape prior. Concretely, the points of initial segmentation result in high confidence when aligning with the implicit template are sampled. The sampled points are firstly input to the fine-tuned INRs to optimize the deformation field and latent codes, and then fed into the fixed INRs of the template network to generate the refined results.

To the best of our knowledge, this work is the first to introduce implicit neural representation to refine initial segmentation results of medical images obtained from CNNs. To validate the effectiveness of the proposed method, we performed extensive experiments on three medical datasets, including liver, pancreas, and lung lobes. Compared to other state-of-the-art voxel-based / coordinate-based approaches, experimental results demonstrate that the proposed method achieved superior quantitative performance with better interpretability.

2. Related Works

2.1. Discrepancy of Natural and Medical Shapes

Deep implicit functions have particularly emerged as a powerful paradigm to represent 3D shapes (Chen and Zhang, 2019; Mescheder et al., 2019; Sitzmann et al., 2020; Peng et al., 2020; Sitzmann et al., 2019; Chabra et al., 2020; Jiang et al., 2020) used in natural 3D shapes or scenes. However, applying deep implicit functions to 3D medical shapes is not straightforward. This is mainly attributed to the discrepancies between medical and natural datasets in shape representation.

First, the continuity of shapes is an obvious difference between natural datasets and medical datasets. Take widely used manufactured objects(Chang et al., 2015) in natural shape modeling as a comparison, they are mainly acquired by computer-aided design systems, and the triangulated meshes are naturally built within shapes. Hence, the continuity can be ensured in the synthetic objects while the situation is not true for medical datasets. As medical shapes are generally annotated on discrete grids slice-by-slice in image stacks, the reconstructed shapes share lower quality than natural shapes due to the high expense of precise annotation in medical images and the limitation of discrete voxel grids(Tajbakhsh et al., 2020; Zhou et al., 2021). Consequently, the continuity of medical shapes is challenging to guarantee.

Second, natural shapes(Chang et al., 2015) provide the physical normalization with rigid alignment, which establishes a consistent canonical orientation for models within each category. This is significant for the coordinate-based learning paradigm of implicit neural fields. On the contrary, the spatial resolution and location of medical shapes are rarely constant and often anisotropic. Therefore, it is necessary to perform the alignment on medical shapes within the same category before the shape modeling by implicit neural fields.

Third, the basic elements of natural shapes are point clouds, while medical datasets are represented using voxels. The implicit neural network requires the point cloud data of the shapes

of interest to serve as the foundational input. To generalize the implicit neural network to unseen data, it needs partial point cloud data of the targeted shapes. This is compatible with natural shape representation while is challenging for medical datasets.

2.2. Deep Implicit Surface Reconstruction

Implicit functions (Carr et al., 2001; Shen et al., 2004) were adopted to represent shapes via constructing volumetric fields and expressing shapes of their iso-surfaces. With the development of deep learning methods, deep implicit functions have been introduced into neural networks as neural fields (Park et al., 2019; Chen and Zhang, 2019; Mescheder et al., 2019; Sitzmann et al., 2020; Peng et al., 2020; Sitzmann et al., 2019) and have emerged as a powerful paradigm. DeepSDF (Park et al., 2019) is a representative method that defines the surface of its shape as the level set of a signed distance field (SDF). Specifically, it defines a neural field, termed \mathcal{F}_{SDF} . For a given spatial point $p \in \mathbb{R}^3$, along with the specific latent code $\alpha \in \mathbb{R}^K$ for each instance, \mathcal{F}_{SDF} takes them as input and output signed distance value, $\mathcal{F}_{\text{SDF}} : \mathbb{R}^{3+K} \rightarrow \mathbb{R}$:

$$\mathcal{F}_{\text{SDF}}(p, \alpha) \in \mathbb{R}^{3+K} = s \in \mathbb{R}, \quad (1)$$

where the absolute value of s denotes the distance to the closet surface, and the sign encodes whether p is inside (negative) and outside (positive) the shape surface. \mathcal{F}_{SDF} is a continuous implicit function since p is given arbitrarily of every possible 3D point rather than discrete 3D locations in voxel representation. With \mathcal{F}_{SDF} , the shape surface can be implicitly represented based on the iso-surface of $\mathcal{F}_{\text{SDF}}(\cdot) = 0$, followed by Marching Cube algorithm(Lorensen and Cline, 1998) to extract the mesh. In addition, some other approaches regarded the continuous implicit function as occupancy probability prediction(Mescheder et al., 2019; Peng et al., 2020; Xu et al., 2019). Recent studies take the consideration of local patterns in the complex shapes/scenes and introduce local implicit functions to capture geometric details(Jiang et al., 2020; Chabra et al., 2020). However, current deep implicit functions focused on the shape reconstruction and completion task, need partial observation data even in unknown shape reconstruction tasks, which limits their generalization ability. Our proposed method overcomes this limitation and first introduces implicit neural representation to refine the initial segmentation results of medical images.

2.3. Latent Constraints for Medical Shape Refinement

Latent constraints are usually adopted for the refinement of initial medical image segmentation. Ricardo *et al.* (Araújo et al., 2019) cascaded a Variational Auto Encoder (Kingma and Welling, 2014) after the FCN to construct the improved topology coherence network (ICTNet). It aims to learn a latent space that is capable of reducing topological incoherence. Jha *et al.* designed two consecutive U-Net structures to construct the Double-UNet(Jha et al., 2020). The output of the first UNet was regarded as the latent features, transported into the second UNet with the multiplication of the origin image. In addition, the features derived from the encoder of the first UNet were

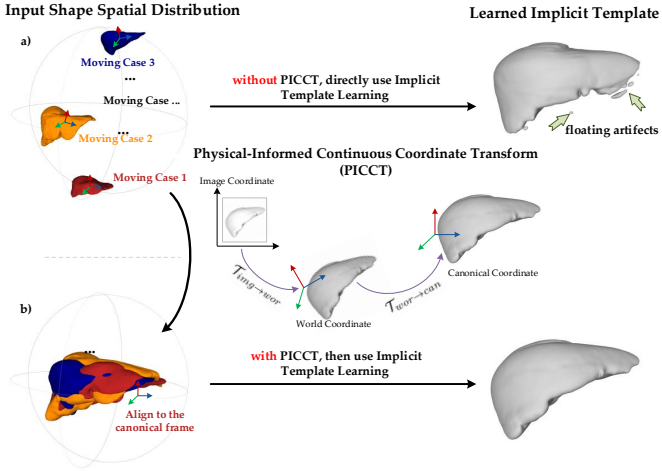


Fig. 2. Comparison of implicit template learning w/ and w/o PICCT.

skip-connected to the decoder of the second UNet, followed by the two concatenated output feature maps obtained from the two corresponding UNets. Dai *et al.* proposed the Structure Correcting Adversarial Network (SCAN) (Dai *et al.*, 2018) to refine organ segmentation. SCAN incorporates an adversarial network with the FCN to better preserve structural regularities inherent in human physiology. Similar to (Isola *et al.*, 2017), the adversarial network maps the prediction and the ground-truth to the latent space, aiming to learn higher order discriminative structures discriminate. Via the adversarial training process, the learned global information spread backward to the FCN to achieve realistic outcomes. SCAN mainly reinforces the FCN to simulate the ground-truth while not designed to learn to correct structural errors based on the shape prior.

Recent works attempted to utilize implicit representation in medical image segmentation (Marimont and Tarroni, 2022; Sørensen *et al.*, 2022; Khan and Fang, 2022). Implicit U-Net (Marimont and Tarroni, 2022) adapted implicit representation paradigm to volumetric medical image segmentation task. They replaced the UNet Decoder branch with an implicit decoder proposed by (Park *et al.*, 2019). It extracted features of a point \mathbf{p} from multiple spatial resolution. The gather layer operates on each resolution of the encoder part to consistently acquire the same size of point-wise feature maps, which are then concatenated along with the original coordinates for the implicit decoder. Kristine *et al.* designed a Neural Unsigned Distance Field (NUDF) (Sørensen *et al.*, 2022), aiming to represent the medical shape surface. Volumetric images are first processed through the encoder part of 3D-UNet to produce feature maps of multiple resolutions. Points are sampled from these feature maps, and then fed into a fully connected neural network to predict the distance from the point to the surface. Khan *et al.* designed an Implicit Organ Segmentation Network (IOSNet) (Khan and Fang, 2022) that utilizes implicit neural representation. Compared with (Marimont and Tarroni, 2022), the point-wise feature maps are not recalibrated to the same size, and the implicit decoder part is more lightweight than the Implicit U-Net. However, (Marimont and Tarroni, 2022; Sørensen *et al.*,

2022; Khan and Fang, 2022) merely added the coordinate-based latent constraint in the segmentation process, which does not particularly break the limitation of discrete voxel grid. Besides, the common structural prior knowledge shared across the same category of medical shapes has not been explored.

3. Methodology

3.1. Physical-Informed Continuous Coordinate Transform

To better explore the meta information (origin, spacing, direction) of the volumetric data in the continuous space, we proposed the Physical-Informed Continuous Coordinate Transformation (PICCT) to align medical shapes into the canonical frame. As mentioned in Sec. 2.1, the majority of medical data is not been rigorously registered. To prevent erroneous learning of the shared shape template as demonstrated in Fig.2.a), we perform PICCT on the medical shapes across the dataset. Specifically, One shape within the dataset is designated as the anchor shape, denoted by \mathcal{A} , the remaining shapes are regarded as moving shapes set, termed as $\{\mathcal{M}\}$. The PICCT aims to find the simple yet effective rigid transformation from each sample of moving shapes \mathcal{M}_i to the anchor shape \mathcal{A} .

$$\mathcal{M}'_i = \mathcal{T}_{\mathcal{M} \rightarrow \mathcal{A}}(\mathcal{M}), \quad (2)$$

where \mathcal{M}'_i denotes the transformed shape, and $\mathcal{T}_{\mathcal{M} \rightarrow \mathcal{A}}$ denotes the concrete PICCT between \mathcal{M}_i and \mathcal{A} . PICCT comprises two components, $\mathcal{T}_{img \rightarrow wor}$ first transforms the image coordinate system to the world coordinate system, then $\mathcal{T}_{wor \rightarrow can}$ transforms the world coordinates to the canonical frame system.

$\mathcal{T}_{\mathcal{M} \rightarrow \mathcal{A}}$ is formulated as $\mathcal{T}_{\mathcal{M} \rightarrow \mathcal{A}} \stackrel{\text{def}}{=} \mathcal{T}_{wor \rightarrow can} \circ \mathcal{T}_{img \rightarrow wor}$. $\mathcal{T}_{img \rightarrow wor}$ takes advantage of the inherent meta information within the volumetric images, transforming the voxel coordinates of the discrete grid space to the world coordinates of the continuous space. The world coordinates can be calculated as:

$$\begin{bmatrix} w_x \\ w_y \\ w_z \end{bmatrix} = \begin{bmatrix} O_x \\ O_y \\ O_z \end{bmatrix} + \begin{bmatrix} D_{x,1} & D_{x,2} & D_{x,3} \\ D_{y,1} & D_{y,2} & D_{y,3} \\ D_{z,1} & D_{z,2} & D_{z,3} \end{bmatrix} * \begin{bmatrix} S_x & 0 & 0 \\ 0 & S_y & 0 \\ 0 & 0 & S_z \end{bmatrix} * \begin{bmatrix} i_x \\ i_y \\ i_z \end{bmatrix}, \quad (3)$$

where $\mathbf{i} = (i_x, i_y, i_z)^T$ denotes the image coordinate, and $\mathbf{w} = (w_x, w_y, w_z)^T$ denotes the world coordinate. $\mathbf{O} \in \mathbb{R}^{3 \times 1}$, $\mathbf{D} \in \mathbb{R}^{3 \times 3}$, $\mathbf{S} \in \mathbb{R}^{3 \times 3}$ represent the origin information, direction information, and spacing information of the volumetric image, respectively. Eq.3 can be transformed into the homogeneous coordinate system, hence, $\mathcal{T}_{img \rightarrow wor}$ is rewritten as:

$$\mathcal{T}_{img \rightarrow wor} = \begin{bmatrix} S_x \cdot D_{x,1} & S_y \cdot D_{x,2} & S_z \cdot D_{x,3} & O_x \\ S_x \cdot D_{y,1} & S_y \cdot D_{y,2} & S_z \cdot D_{y,3} & O_y \\ S_x \cdot D_{z,1} & S_y \cdot D_{z,2} & S_z \cdot D_{z,3} & O_z \\ 0 & 0 & 0 & 1 \end{bmatrix}. \quad (4)$$

After acquiring the world coordinates of the shapes, we perform the rigid transformation calculation that registers the moving

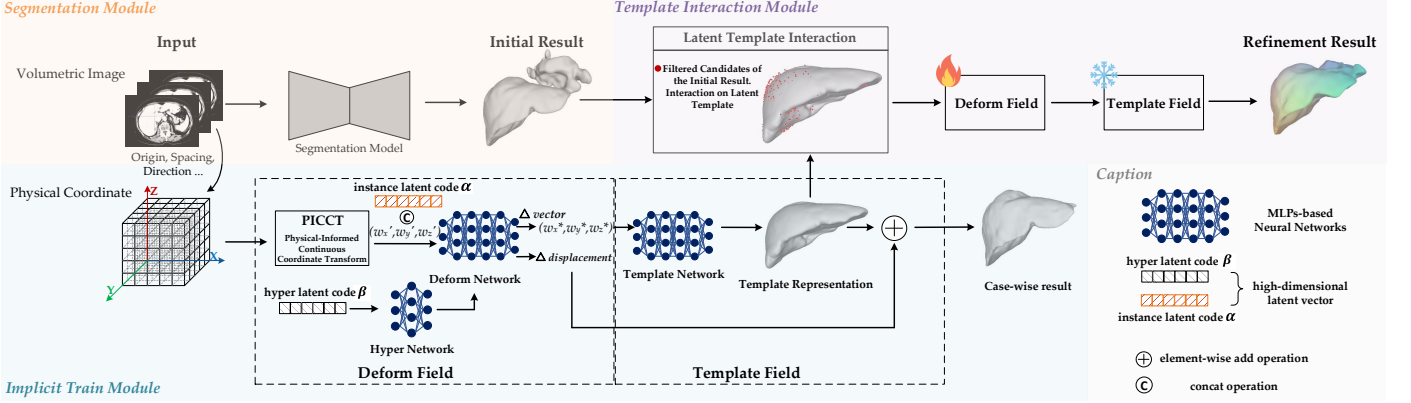


Fig. 3. Overview of the proposed implicit shape modeling framework for anatomical structure refinement of volumetric data. a) In the implicit training module, the aligned coordinates w' along with corresponding latent code α are fed into the implicit deformation field $Deform$ followed by one implicit template field $Temp$ to construct implicit shape modeling of medical anatomical structures. The $Deform$ is driven by a hypernetwork $\mathcal{H}(\beta)$ to better fuse w' and α . b) Template interaction module (TIM) integrates the shape of prior knowledge learned from continuous space into the initial results generated by the segmentation head. TIM filters top-matched points according to the implicit template and then finetunes the case-wise latent code α and implicit deformation field $Deform$ to achieve refined results.

shapes into the anchor shape, i.e., canonical frame:

$$\begin{bmatrix} w'_x \\ w'_y \\ w'_z \\ 1 \end{bmatrix} = \begin{bmatrix} s \mathbf{R} & \mathbf{t} \\ 0 & 1 \end{bmatrix} * \begin{bmatrix} w_x \\ w_y \\ w_z \\ 1 \end{bmatrix}, \quad (5)$$

where $w' = (w'_x, w'_y, w'_z)^T$ represents the aligned world coordinates, and $\mathcal{T}_{wor \rightarrow can}$ can be denoted as:

$$\mathcal{T}_{wor \rightarrow can} = \begin{bmatrix} s \mathbf{R} & \mathbf{t} \\ 0 & 1 \end{bmatrix}, \quad (6)$$

where $\mathbf{R} \in \mathbb{R}^{3 \times 3}$, $\mathbf{t} \in \mathbb{R}^{3 \times 1}$, and s denotes the rotation matrix, translation vector, and scaling factor, respectively. The rigid transformation $\mathcal{T}_{wor \rightarrow can}$ is derived based on the Coherent Point Drifting (CPD) algorithm (Myronenko and Song, 2010). In brief, the point set of world coordinates from a moving shape ($\mathbf{W}^{Mov} \in \mathbb{R}^{M \times 3}$) is regarded as Gaussian Mixture Model (GMM) centroids, and the point set of world coordinates from the anchor shape ($\mathbf{W}^{Anc} \in \mathbb{R}^{N \times 3}$) is represented as data points. The CPD mainly fits the GMM centroids to the data points by minimizing the negative log-likelihood function:

$$\begin{aligned} & \min_{\mathbf{R}, \mathbf{t}, s, \sigma^2} \sum_{m,n=1}^{M,N} P(m|W_n^{Anc}) \|W_n^{Anc} - s\mathbf{R}W_m^{Mov} - \mathbf{t}\|^2 \\ & + \frac{3}{2} \sum_{m,n=1}^{M,N} P(m|W_n^{Anc}) \log \sigma^2, \text{ s.t. } \mathbf{R}^T \mathbf{R} = \mathbf{I}, \det(\mathbf{R}) = 1. \end{aligned} \quad (7)$$

$P(m|W_n^{Anc})$ is the posterior probability of the GMM centroid given the data point. Eq.7 is optimized by Expectation Maximization (EM) (Bishop, 1995; Myronenko and Song, 2009) and Singular Value Decomposition (SVD) (Dempster et al., 1977) algorithms. The PICCT roughly assigns the correspondence between moving medical shapes and the anchor shape, and then aligns them into the canonical frame in the continuous world coordinate system, as seen in Fig.2.b).

3.2. Implicit Shape Modeling with Template Generation

After acquiring the coordinates of medical shapes in the canonical frame, we then introduce the implicit shape modeling with template generation of medical anatomical structures. It is well-acknowledged that the same category of medical shapes shares similar anatomical structures (Wang et al., 2012; Iglesias and Sabuncu, 2015). For example, the liver structure can be divided into liver right lobe, liver left lobe, and the inferior hepatic margin. The pancreas shares the head, body, and tail parts. Inspired by (Zheng et al., 2021; Deng et al., 2021), we decompose the paradigm of Deepsdf (Park et al., 2019) (as seen in Eq.1) into one implicit deformation field followed by one implicit template field (Deform-Template) to construct implicit shape modeling of medical anatomical structures. As illustrated in Fig.3, each object is assigned by a learnable n-dimensional latent vector $\alpha \in \mathbb{R}^n$ to encode the desired instance shape. Conceptually, we map the instance latent vector α , concatenated with the aligned shape coordinate w' to the Deform-Template implicit field based on the continuous SDF. Considering that the coordinates w' of different shapes are pre-processed by the PICCT, while instance latent vectors are directly initialized from the same Gaussian distribution, $\mathcal{N}(0, 0.01^2)$ rather than be conditioned. To encourage the weights of the deformation field to be instance-specific, we introduce an additional hyper latent code $\beta \in \mathbb{R}^n \sim \mathcal{N}(0, 0.01^2)$ to form a hyper-network $\mathcal{H}(\beta)$, similar to (David et al., 2017). $\mathcal{H}(\beta)$ aims to generate the weights of the deformation field and can be viewed as additional conditions to fuse α and w' . The overall design of Deform-Template implicit function, \mathcal{F}_{D-T} , can be represented as:

$$\mathcal{F}_{D-T}(w', \alpha, \beta) = Temp \circ Deform(w', \alpha, \beta) \rightarrow s \in \mathbb{R}, \quad (8)$$

where $\mathcal{F}_{D-T} : (w', \alpha, \beta) \in \mathbb{R}^{3+n} \times \mathbb{R}^n \rightarrow s \in \mathbb{R}$. \mathcal{F}_{D-T} is a composite function formed by two implicit networks, $Deform$ and $Temp$. The weights of $Deform$ are derived by the hyper-

network \mathcal{H} :

$$\mathcal{H} : \beta \in \mathbb{R}^n \rightarrow Deform_{layer^i} \in \mathbb{R}^d. \quad (9)$$

Both *Temp* and *Deform* are implemented by Multilayer Perceptrons (MLPs). \mathcal{H} comprises a set of MLPs, each responsible for the weights of a single fully-connected layer i within *Deform*, as illustrated in Eq.9. We abbreviate the parameterized *Deform* as $Deform_{\mathcal{H}(\beta)}$ in the following description.

$Deform_{\mathcal{H}(\beta)}$ takes the instance latent vector α and aligned shape coordinate \mathbf{w}' as input and transformed them to the latent template space by predicting the deformation flow vector field Δvec and scalar displacement field Δdis :

$$Deform_{\mathcal{H}(\beta)} : (\mathbf{w}', \alpha) \in \mathbb{R}^{3+n} \rightarrow (\Delta vec \in \mathbb{R}^3, \Delta dis \in \mathbb{R}). \quad (10)$$

Δvec denotes the per-point spatial offset that deforms the instance to the template space. The transformed coordinate can be calculated by $\mathbf{w}' + \Delta vec$, which is subsequently fed into the *Temp* to acquire the SDF value in the template space:

$$Temp : (\mathbf{w}' + \Delta vec) \in \mathbb{R}^3 \rightarrow \hat{s} \in \mathbb{R}, \quad (11)$$

where the \hat{s} stands for the mapped SDF value of the instance in the template space. Δdis is the per-point displacement to handle anatomical variations. It is added into the \hat{s} to obtain instance-specific SDF value s . Hence, Eq.8 can be rewritten as:

$$\begin{aligned} s &= \mathcal{F}_{D-T}(\mathbf{w}', \alpha, \beta) = Temp(\mathbf{w}' + \Delta vec) + \Delta dis \\ &= Temp(\mathbf{w}', Deform_{\mathcal{H}(\beta)}^{\Delta vec}(\mathbf{w}', \alpha)) + Deform_{\mathcal{H}(\beta)}^{\Delta dis}(\mathbf{w}', \alpha). \end{aligned} \quad (12)$$

Given the training shapes, we apply the SDF regression combined with SDF function attributes as constraints to learn continuous SDFs of these shapes, $\mathcal{F}_{D-T}(\mathbf{w}', \alpha, \beta)$ is the predicted SDF value and the objective function can be defined as follows:

$$\begin{aligned} \mathcal{L}_{sdf} &= \sum_i (\omega_s \sum_{\mathbf{w}' \in \Omega_i} |\mathcal{F}_{D-T}(\mathbf{w}', \alpha, \beta) - \mathbf{s}(\mathbf{w}')| + \\ &\quad \omega_n \sum_{\mathbf{w}' \in S_i} (1 - S_{\cos}(\nabla \mathcal{F}_{D-T}(\mathbf{w}', \alpha, \beta), \mathbf{n}(\mathbf{w}')))) + \\ &\quad \omega_{Eik} \sum_{\mathbf{w}' \in \Omega_i} |||\nabla \mathcal{F}_{D-T}(\mathbf{w}', \alpha, \beta)||_2 - 1| + \\ &\quad \omega_\phi \sum_{\mathbf{w}' \in \Omega_i \setminus S_i} \phi(\mathcal{F}_{D-T}(\mathbf{w}', \alpha, \beta)), \end{aligned} \quad (13)$$

where $\mathbf{s}(\mathbf{w}')$ and $\mathbf{n}(\mathbf{w}')$ indicate the ground-truth of SDF and surface normal value, respectively. Ω_i denotes the 3D shape space of the i^{th} instance, and S_i is the corresponding shape surface. In fact, points will be sampled both on the surface and free space to calculate \mathcal{L}_{sdf} . The first term in Eq.13 directly supervises the SDF regression results. The second term illustrates the surface normal constraint. ∇ represents the spatial gradient of the neural field, and the gradient function of the SDF equals the surface normal. The cosine similarity (S_{\cos}) between gradient function and surface normal ground-truth is adopted to supervise the normal consistency. The third term enforces the amplitude of the SDF gradient function to be 1 as determined by the Eikonal equation (Osher et al., 2004). The last term penalizes off-surface

points with SDF prediction to zero: $\phi(s) = \exp(-\delta \cdot \|s\|)$, $\delta \gg 1$. $\omega_s, \omega_n, \omega_{Eik}, \omega_\phi$ are weighting terms used in \mathcal{L}_{sdf} .

With \mathcal{F}_{D-T} , the 3D medical anatomical shape is represented by an implicit template field that is shared across the same category. The shape variance is captured by the implicit deformation field, which includes the deformation flow vector field and scalar displacement field for instance-specific shape modeling. \mathcal{F}_{D-T} takes advantage of inducing correspondences between implicit template and object instances as well as the correspondences across different objects. This benefits the shape modeling procedure since it focuses on the intrinsic anatomical structure, which could provide useful structural prior guidance for the refinement of medical image segmentation.

3.3. Template Interaction Module

The implicit shape modeling, along with the template generation, learns the shape prior knowledge from anatomical structures in the continuous space. To generalize to the unseen volumetric data, we propose the Template Interaction Module (TIM) to integrate the shape prior knowledge into the initial results generated by pretrained CNNs. CNNs (Çiçek et al., 2016) own the inductive bias ability of CNNs to generalize to unseen medical images. However, the discrete grid-wise and patch-wise learning paradigms are hard to learn intrinsic anatomical knowledge. Implicit shape modeling breaks through the limitation of the discrete grid, learning shape prior knowledge in a continuous and patch-free fashion. Hence, the proposed TIM is suitable to interact with the predicted results by CNNs with the learned implicit template for anatomical structure refinement. Concretely, the initial result is first processed by PICCT ($\mathcal{T}_{wor \rightarrow can} \circ \mathcal{T}_{img \rightarrow wor}$) to map to the canonical frame. Second, we perform the align operation between the aligned initial result and the learned template based on Eq.7, denoting as $\mathcal{T}_{init \rightarrow temp}$. The intermediate transformation matrix $\mathbf{P}_{IT} \in \mathbb{R}^{I \times T}$ is applied to select the matching points. $\mathbf{P}_{IT} \in \mathbb{R}^{I \times T}$ denotes the alignment probability from the initial result to the template result, where $P_{I=i, T=t}$ indicates the probability that align the i^{th} point of the initial result to the t^{th} point of the template shape. Next, we aggregate the alignment probability of each point in the initial result to all points in the template shape: $\mathbf{P}_I = \mathbf{P}_{IT} \mathbf{1}$. Then, the Top K % of points in \mathbf{P}_I are obtained for the subsequent implicit refinement. As seen in Fig.3, TIM interacts initial results with the learned template, enabling the generalization of the implicit neural networks. The filtered top-matched points could reduce the structural errors made in CNNs and improve the learning efficiency in the refinement stage.

3.4. Model Optimization Pipeline

During the training stage, not only \mathcal{L}_{sdf} is optimized to learn continuous SDF functions, but also additional constraints are introduced to facilitate the implicit shape modeling with template generation. First, to optimize the implicit template to share common structures of the specific category, we add the normal direction constraints of points in the template space to be consistent with the corresponding given shape:

$$\mathcal{L}_{tpn} = \omega_n \sum_i \sum_{\mathbf{w}' \in S_i} (1 - S_{\cos}(\nabla Temp(\mathbf{w}' + \Delta vec), \mathbf{n}(\mathbf{w}'))). \quad (14)$$

Further, to prohibit the large shape distortion caused by Δvec and large displacement Δdis , we design two regularization terms, \mathcal{L}_{vec} and \mathcal{L}_{dis} to constrain $Deform_{\mathcal{H}(\beta)}$. \mathcal{L}_{vec} aims to achieve smooth deform flow between the specific instance and the latent template. We add Laplacian smooth constraint to the Δvec :

$$\begin{aligned}\mathcal{L}_{vec} &= \sum_i \sum_{\mathbf{w}' \in \Omega_i} \left\| \nabla \cdot \nabla Deform_{\mathcal{H}(\beta)}^{\Delta vec}(\mathbf{w}', \alpha) \right\|_2 \\ &= \sum_i \sum_{\mathbf{w}' \in \Omega_i} \left\| \frac{\partial^2 D_{\mathcal{H}(\beta)}^{\Delta vec}}{\partial x^2} + \frac{\partial^2 D_{\mathcal{H}(\beta)}^{\Delta vec}}{\partial y^2} + \frac{\partial^2 D_{\mathcal{H}(\beta)}^{\Delta vec}}{\partial z^2} \right\|_2,\end{aligned}\quad (15)$$

$D_{\mathcal{H}(\beta)}^{\Delta vec}$ is the short notion for $Deform_{\mathcal{H}(\beta)}^{\Delta vec}(\mathbf{w}', \alpha)$ in Eq.15. In addition, \mathcal{L}_{dis} aims to reduce the amplitude of displacement Δdis , enhancing the accuracy of implicit template and correspondence:

$$\mathcal{L}_{dis} = \sum_i \sum_{\mathbf{w}' \in \Omega_i} \left| Deform_{\mathcal{H}(\beta)}^{\Delta dis}(\mathbf{w}', \alpha) \right|. \quad (16)$$

We also assign the regularization loss to the latent codes α and β as in (Park et al., 2019).

$$\mathcal{L}_{reg.\alpha} = \sum_i \|\alpha_i\|_2^2. \quad (17)$$

$$\mathcal{L}_{reg.\beta} = \sum_i \|\beta_i\|_2^2. \quad (18)$$

In summary, the whole training optimization of the implicit modeling can be defined as:

$$\begin{aligned}\arg \min_{\{\alpha, Deform_{\mathcal{H}(\beta)}, Temp\}} & \mathcal{L}_{sdf} + \mathcal{L}_{tpn} + \omega_{vec} \mathcal{L}_{vec} + \omega_{dis} \mathcal{L}_{dis} \\ & + \omega_{\alpha} \mathcal{L}_{reg.\alpha} + \omega_{\beta} \mathcal{L}_{reg.\beta},\end{aligned}\quad (19)$$

where ω_{vec} , ω_{dis} , ω_{α} , ω_{β} are the weighting terms. As for the refinement stage, given a pretrained segmentation model, the initial result can be obtained. Meanwhile, the learned implicit template is fixed at this stage. To embed the test shape to the latent space, specific instance latent code and deform field fine-tuned for the refinement usage:

$$\arg \min_{\{\alpha, Deform_{\mathcal{H}(\beta)}\}} \mathcal{L}_{sdf} + \omega_{\alpha} \mathcal{L}_{reg.\alpha} + \omega_{\beta} \mathcal{L}_{reg.\beta}. \quad (20)$$

4. Experiments and results

4.1. Data

4.1.1. Datasets

We evaluated our method on three public datasets listed as follows:

MSD Liver Dataset. The liver dataset from the Medical Segmentation Decathlon (MSD) (Antonelli et al., 2022) was used in our experiments. It contains 131 CT images in total, 91 CT images for training, 13 CT images for validation, and 27 CT images for testing. The in-plane resolution ranges from 0.5 to 1.0 mm, and the slice thickness ranges from 0.45 to 6.0 mm. The

pixel values were clipped to [-100, 400] HU, and normalized to [0, 255].

NIH Pancreas-CT Dataset. The pancreas dataset (Roth et al., 2015) contains 80 abdominal contrast enhanced 3D CT scans. 56 CT images for training, 8 CT images for validation, and 16 CT images for testing. The in-plane resolution ranges from 0.66 to 0.98 mm, and the slice thickness varies from 1.5 to 2.5 mm. The pixel values were clamped to [-100, 240] HU, before rescaled to [0, 255].

Lung Lobe Dataset. The lung lobe dataset (Tang et al., 2019) that contains five lobes annotations was used in our experiments. It contains 50 CT scans, 35 CT images for training, 5 CT images for validation, and 10 CT images for testing. The in-plane resolution ranges from 0.54 to 0.88 mm, and the slice thickness varies from 0.625 to 2.5 mm. The pixel values were clamped to [-1000, 600] HU, before rescaled to [0, 255].

4.1.2. Data Preparation

The data preparation for implicit shape modeling should sample appropriate points with corresponding SDF values. Since all medical shapes are annotated as 3D volumes, we first extracted the surface mesh via Marching Cube algorithm (Lorenson and Cline, 1998). After the execution of PICCT on each surface mesh, we followed a similar process of (Park et al., 2019) to randomly sample points on the surface mesh and in the free space. Concretely, we first normalized each surface mesh to the unit sphere. Next, for surface points sampling, 100 virtual images were rendered for each normalized mesh from 100 virtual cameras. Surface points were acquired through back-projecting the depth pixels, and the corresponding normals were assigned from the triangle to which it belongs. As for free space points sampling, we sampled them in the unit sphere uniformly and calculated the distance to the nearest surface. The sign of the distance was decided based on the depth with regard to the surface points. As long as the free points had a smaller depth value in any virtual image, it was assigned a positive sign, otherwise, it got a negative sign. In summary, 800K surface points along with normals and 200K free space points with corresponding SDF values were sampled for each shape.

4.2. Implementation Details

4.2.1. Network Architecture Details

Both the implicit neural network $Temp$ and $Deform$ were implemented by the MLPs. The dimension of instance latent code α and hyper latent code β were set to 256. The hyper-network $\mathcal{H}(\beta)$ consists of multiple 3-layer MLPs, each responsible for the weights of a single fully-connected layer i within the implicit neural network $Deform$. The hidden feature is 256 in hyper-network $\mathcal{H}(\beta)$. Both $Temp$ and $Deform$ owns 5 fully-connected layers, of which the hidden feature was also set to 256. Sine activations were adopted in both $Temp$ and $Deform$ as proposed by (Sitzmann et al., 2020). Initialization of weights was also obeyed (Sitzmann et al., 2020). α and β were initialized using $\mathcal{N}(0, 0.01^2)$. ReLU activations were adopted in $\mathcal{H}(\beta)$, and be initialized using (He et al., 2015).

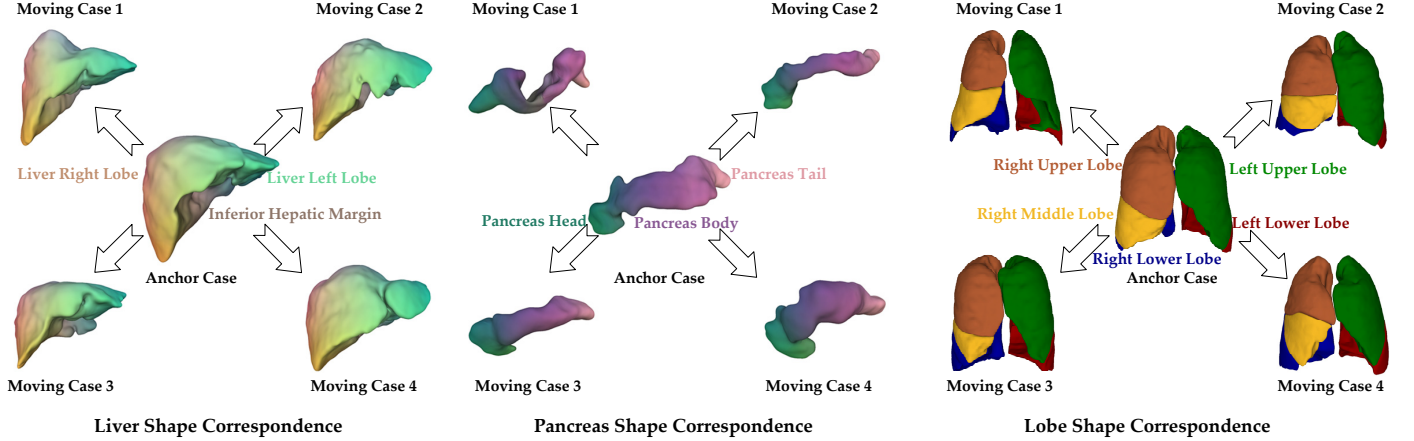


Fig. 4. Demonstration of shape representation ability. Implicit shape modeling builds up dense correspondences in the continuous space across instances within the same category. The template shape has learned critical parts of anatomical structures, which is helpful to transfer the shape prior knowledge to the refinement usage. Correspondences are shown with the same colors.

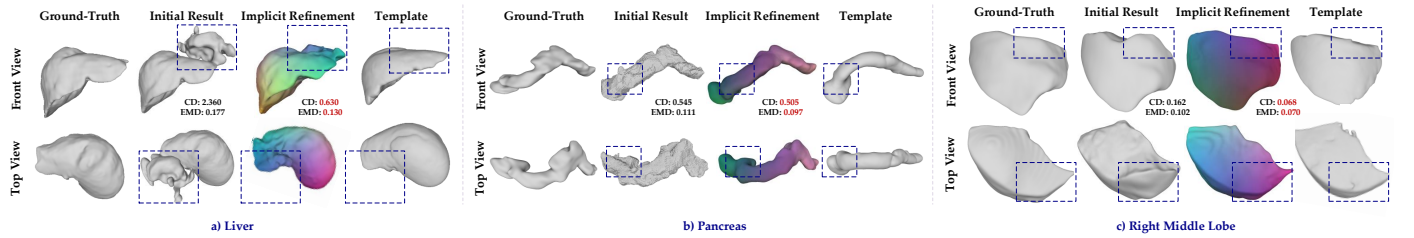


Fig. 5. Examples of the refinement results on the Liver, Pancreas, and Right Middle Lobe. The dotted blue boxes highlight the same areas in the initial results, implicit refinement results, and template space. a) Structural error has been corrected according to the template. b) Staircase artifact of the boundary has been refined. c) The misclassification problem has been alleviated.

4.2.2. Training and Finetune Details

As for the training procedure, we jointly optimized all instance-wise latent codes α , $\mathcal{H}(\beta)$, and $Temp$ based on Eq.19. The setting of weighting terms in \mathcal{L}_{sdf} were followed by (Sitzmann et al., 2020), ω_s , ω_n , ω_{Eik} , and ω_ϕ were set to $3e3$, $1e2$, $5e1$, and $5e2$ respectively. $\omega_{vec} = 5.0$, $\omega_{dis} = 1e2$, $\omega_\alpha = 1e5$, and $\omega_\beta = 1e6$ was used in the training progress. For each iteration, 4K surface points and 4K free-space points for each shape were randomly sampled for optimization. The Adam optimizer (Kingma and Ba, 2014) with a learning rate of $1e-4$ and a batchsize of 16 were adopted. 200 epochs were trained in total. As for the finetune stage, since the implicit template field $Temp$ is shared across the class, we fixed its weight and adopted the learned template for interaction usage. The top K % used in TIM module was set to Top 25 %. α and $\mathcal{H}(\beta)$ were finetuned via Eq.20 for 30 epochs. Other settings were identical to the training procedure. We adopted the PyTorch framework to implement all experiments, which were executed on a Linux workstation with Intel Xeon Gold 5218 CPU @ 2.30 HZ, 128GB RAM, and 2 NVIDIA Geforce RTX 3090 GPUs.

4.2.3. Evaluation Metrics

The principal metric of concern in this study is the quality of the shape surface that is refined by implicit neural networks in the continuous space. Chamfer Distance (CD) (Fan et al.,

2017) and Earth Mover’s Distance (EMD) (Rubner et al., 1998) are two appropriate metrics to measure shapes represented by meshes. These two metrics are calculated on two point sets S_1 and S_2 that are sampled from the surfaces of refined shape and ground-truth respectively. The CD can be defined as:

$$CD \stackrel{\text{def}}{=} d_{CD}(S_1, S_2) = \sum_{x \in S_1} \min_{y \in S_2} \|x - y\|_2 + \sum_{y \in S_2} \min_{x \in S_1} \|y - x\|_2. \quad (21)$$

In all experiments, we used 30K points for both S_1 and S_2 , and reported CD by the normalized result: $\frac{d_{CD}(S_1, S_2)}{30,000}$. With regard to the EMD (Rubner et al., 1998), which forms a bijection: $\phi : S_1 \rightarrow S_2$. The EMD is defined based on the optimal bijection:

$$EMD \stackrel{\text{def}}{=} d_{EMD}(S_1, S_2) = \min_{\phi: S_1 \rightarrow S_2} \sum_{x \in S_1} \|x - \phi(x)\|_2. \quad (22)$$

We adopted 1K points to calculate EMD in all experiments. In addition, benefiting from the invertibility of PICCT, we could perform $\mathcal{T}_{img \rightarrow wor}^{-1} \circ \mathcal{T}_{wor \rightarrow can}^{-1}$ on the refined shapes in the continuous space to map back to the discrete voxel space. Specifically, the refined shape mesh should be subdivided and conducted the inverse transform of PICCT to acquire the boundary of the volumetric shapes first. Next, the areas inside the boundary are filled to obtain the volume results. Hence, the sec-

Table 1. Quantitative comparison of the Liver, Pancreas, and Lung Lobe datasets in the continuous metric space. CD = Chamfer Distance, multiplied by 10^2 . EMD = Earth Mover’s Distance.

Liver Dataset				
Method	CD (mean. \pm std.) \downarrow	EMD (mean. \pm std.) \downarrow	CD (median) \downarrow	EMD (median) \downarrow
Double-UNet (Jha et al., 2020)	2.823 \pm 1.779	0.184 \pm 0.047	2.912	0.196
SCAN (Dai et al., 2018)	2.125 \pm 1.319	0.166 \pm 0.049	2.304	0.177
ICTNet (Araújo et al., 2019)	0.504 \pm 1.233	0.146 \pm 0.037	0.802	0.123
Implicit U-Net (Marimont and Tarroni, 2022)	0.536 \pm 0.396	0.119 \pm 0.018	0.512	0.110
NUDF (Sørensen et al., 2022)	0.579 \pm 0.774	0.118 \pm 0.030	0.122	0.103
IOSNet (Khan and Fang, 2022)	1.820 \pm 1.542	0.160 \pm 0.048	1.096	0.157
Proposed	0.232 \pm 0.374	0.087 \pm 0.021	0.086	0.081
Pancreas Dataset				
Method	CD (mean. \pm std.) \downarrow	EMD (mean. \pm std.) \downarrow	CD (median) \downarrow	EMD (median) \downarrow
Double-UNet (Jha et al., 2020)	1.084 \pm 0.227	0.114 \pm 0.067	0.154	0.089
SCAN (Dai et al., 2018)	0.240 \pm 0.217	0.087 \pm 0.018	0.157	0.081
ICTNet (Araújo et al., 2019)	0.578 \pm 1.246	0.100 \pm 0.045	0.191	0.086
Implicit U-Net (Marimont and Tarroni, 2022)	2.190 \pm 0.317	0.144 \pm 0.083	0.906	0.120
NUDF (Sørensen et al., 2022)	0.310 \pm 0.282	0.093 \pm 0.024	0.237	0.091
IOSNet (Khan and Fang, 2022)	1.084 \pm 2.554	0.106 \pm 0.068	0.334	0.090
Proposed	0.128 \pm 0.106	0.069 \pm 0.024	0.101	0.059
Lung Lobe Dataset				
Method	CD (mean. \pm std.) \downarrow	EMD (mean. \pm std.) \downarrow	CD (median) \downarrow	EMD (median) \downarrow
Double-UNet (Jha et al., 2020)	0.792 \pm 1.083	0.118 \pm 0.036	0.324	0.107
SCAN (Dai et al., 2018)	0.772 \pm 1.020	0.120 \pm 0.034	0.511	0.111
ICTNet (Araújo et al., 2019)	0.746 \pm 1.119	0.120 \pm 0.036	0.426	0.109
Implicit U-Net (Marimont and Tarroni, 2022)	0.809 \pm 0.943	0.122 \pm 0.036	0.420	0.113
NUDF (Sørensen et al., 2022)	0.737 \pm 1.006	0.117 \pm 0.037	0.285	0.106
IOSNet (Khan and Fang, 2022)	0.869 \pm 0.822	0.127 \pm 0.030	0.526	0.124
Proposed	0.417 \pm 0.631	0.100 \pm 0.034	0.162	0.090

ondary volume-based metrics are also included to compare the proposed approach with other state-of-the-art methods. We reported Dice Similarity Coefficient (DSC, %), Normalized Surface Dice (Nikolov et al., 2018) (NSD, %), 95% Hausdorff distance (HD95, mm), and Average symmetric surface distance (ASSD, mm) in the quantitative analysis.

4.3. Analysis of Implicit Shape Representation

As illustrated in Fig.4, Implicit shape modeling with template generation can build up dense correspondences in the continuous space across instances within the same category. This deep implicit modeling process in the continuous physical space ensures the robust and automatic establishment of correspondence across instances, which can avoid the need for SSMs to pre-define the correspondence relationship. Take the correspondence of liver shape as an example, different critical parts, in-

cluding the liver left lobe, liver right lobe, and inferior hepatic margin have been discriminated in the implicit shape modeling in a specific instance. Further, correspondences of the same parts from different instances are learned by the implicit neural networks, as shown with the same colors. This observation validates that a collection of medical anatomical shapes share some common structures. These anatomical structure priors can be modeled by implicit neural networks and then used as guidance to refine initial results generated by CNNs.

4.4. Analysis of Implicit Shape Refinement

The standard 3D UNetÇiçek et al. (2016) was chosen as the segmentation model. Equipped with the implicit shape modeling, the results can be refined from an average 0.407 CD / 0.113 EMD to 0.232 CD / 0.087 EMD on the Liver dataset, from 0.223 CD / 0.097 EMD to 0.128 CD / 0.069 EMD on the

Table 2. Quantitative comparison of multi-class lobe dataset in continuous metric space and voxel-wise metric space.

Five Lung Lobes Results																				
Method	CD (mean) ↓					EMD (mean) ↓					CD (median) ↓					EMD (median) ↓				
	RU	RM	RL	LU	LL	RU	RM	RL	LU	LL	RU	RM	RL	LU	LL	RU	RM	RL	LU	LL
Double-UNet	0.660	1.320	0.848	0.286	0.844	0.117	0.142	0.126	0.093	0.114	0.346	1.265	0.262	0.078	0.192	0.107	0.145	0.115	0.087	0.096
SCAN	0.605	1.361	0.774	0.272	0.846	0.119	0.142	0.127	0.097	0.113	0.563	1.024	0.382	0.100	0.198	0.111	0.136	0.118	0.092	0.098
ICTNet	0.498	1.467	0.600	0.249	0.917	0.114	0.150	0.124	0.095	0.115	0.438	1.539	0.276	0.119	0.139	0.106	0.156	0.115	0.098	0.106
Implicit U-Net	0.686	1.367	0.707	0.403	0.081	0.125	0.142	0.125	0.096	0.100	0.410	1.064	0.226	0.107	0.186	0.115	0.135	0.106	0.092	0.097
NUDF	0.587	1.885	0.524	0.272	0.416	0.115	0.158	0.115	0.095	0.100	0.410	1.064	0.226	0.107	0.186	0.115	0.135	0.106	0.092	0.097
IOSNet	0.999	1.352	0.742	0.572	0.679	0.132	0.142	0.132	0.105	0.122	0.458	0.932	0.685	0.202	0.526	0.124	0.125	0.125	0.098	0.117
Proposed	0.462	1.020	0.181	0.176	0.245	0.103	0.124	0.096	0.081	0.095	0.285	0.650	0.178	0.030	0.113	0.095	0.116	0.096	0.075	0.079
Method	DSC (%) ↑					NSD (%) ↑					HD95 (mm) ↓					ASSD (mm) ↓				
	RU	RM	RL	LU	LL	RU	RM	RL	LU	LL	RU	RM	RL	LU	LL	RU	RM	RL	LU	LL
Double-UNet	92.62	83.98	95.03	95.76	95.36	78.27	68.51	85.59	91.13	89.73	16.37	21.26	15.55	11.32	15.35	2.44	3.92	1.88	1.22	1.57
SCAN	92.57	84.41	95.14	95.37	95.08	81.19	70.73	86.42	89.79	89.52	13.68	21.14	16.30	11.90	15.89	2.05	3.72	1.73	1.32	1.68
ICTNet	92.39	83.78	95.34	96.04	95.43	82.14	69.22	86.88	90.36	90.44	13.69	25.03	17.70	10.03	15.35	2.05	4.12	1.84	1.22	1.75
Implicit U-Net	91.98	75.38	94.34	93.78	92.48	78.69	62.61	84.32	86.58	86.31	19.99	20.49	15.87	15.95	19.85	3.22	4.85	2.03	2.21	2.44
NUDF	92.57	84.98	86.25	95.77	96.05	80.72	69.92	89.75	91.67	92.06	24.04	36.70	14.77	13.73	9.56	2.77	5.14	1.40	1.37	1.18
IOSNet	90.30	72.89	91.56	91.57	89.00	73.65	59.13	78.29	78.24	77.86	21.98	21.83	19.95	22.64	21.55	4.10	5.30	2.89	3.34	4.00
Proposed	93.66	84.96	96.45	96.35	96.17	81.67	70.33	90.42	94.28	93.42	14.54	19.09	10.05	7.04	8.46	2.34	3.58	1.04	1.02	1.04

Pancreas dataset, and from 0.677 CD / 0.115 EMD to 0.417 CD / 0.100 EMD on the Lung Lobe dataset. To further investigate the effectiveness of the refinement brought from implicit shape modeling, we provided visualization examples of the refinement results on the Liver, Pancreas, and Right Middle Lobe in Fig.5. The dotted blue boxes highlighted the refined areas, same spatial location in the initial result, implicit refinement result, and template space. The CD and EMD were also decreased upon the implicit refinement. According to the learned template, the succeeding implicit refinement could alleviate the structural errors, staircase artifacts, and misclassification problem.

In addition, recent voxel-wise refinement methods(Araújo et al., 2019; Jha et al., 2020; Dai et al., 2018) and implicit-based segmentation methods (Marimont and Tarroni, 2022; Sørensen et al., 2022; Khan and Fang, 2022) were adopted for comparisons in our experiments:

- **Double-UNet** Jha et al. (2020) designed two consecutive UNet structures to construct the Double-UNet. The second UNet adopts the element-wise multiplication of the origin image and output of the first UNet as the input. In addition, the features derived from the encoder of the first UNet were skip-connected to the decoder of the second UNet, followed by the two concatenated output feature maps obtained from the two corresponding UNets.
- **SCAN** Dai et al. (2018) proposed the Structure Correcting Adversarial Network (SCAN) to refine organ segmentation. SCAN incorporates an adversarial network with the Fully Convolutional Network (FCN) to better preserve structural regularities inherent in human physiology. Similar to Isola et al. (2017), the adversarial network aims to learn higher order structures discriminate between the ground-truth from the prediction generated by FCN. Via adversarial training process, the learned global information spread backward to the FCN to achieve re-

alistic outcomes.

- **ICTNet** Araújo et al. (2019) improved topology coherence network (ICTNet) to correct topological incoherence. A Variational Auto Encoder Kingma and Welling (2014) was cascaded after the FCN. The VAE was cascaded by the segmentation produced by FCN and then reconstructed more precision result, aiming to learn a latent space that is capable of reducing topological incoherence.
- **Implicit U-Net** Marimont and Tarroni (2022) adapted the implicit representation paradigm to medical image segmentation task. They replaced the UNet Decoder branch with an implicit decoder proposed by Park et al. (2019). The Implicit U-Net extracted features of a point \mathbf{p} from multiple spatial resolution. The gather layer operates on each resolution of the encoder part to consistently acquire the same size of point-wise feature maps, which are then concatenated along with the original coordinates for the implicit decoder.
- **NUDF** Sørensen et al. (2022) designed a Neural Unsigned Distance Field (NUDF), aiming to represent the surface in the continuous space rather than voxel grids. Volumetric images are first processed through the encoder part of 3D-UNet to produce feature maps of multiple resolutions. Continuous points are sampled from these feature maps, and then fed into a fully connected neural network to predict the distance from the point to the surface.
- **IOSNet** Khan and Fang (2022) designed an Implicit Organ Segmentation Network (IOSNet) that shares similar ideas with Implicit U-Net while has several differences in the network design: 1) The point-wise feature maps are not recalibrated to the same size. More point features are produced in deeper layers. 2) The implicit decoder part is more lightweight than the Implicit U-Net.

Table 1 and Table 2 report the quantitative results on the shape modeling of unseen CT data with regard to the measure-

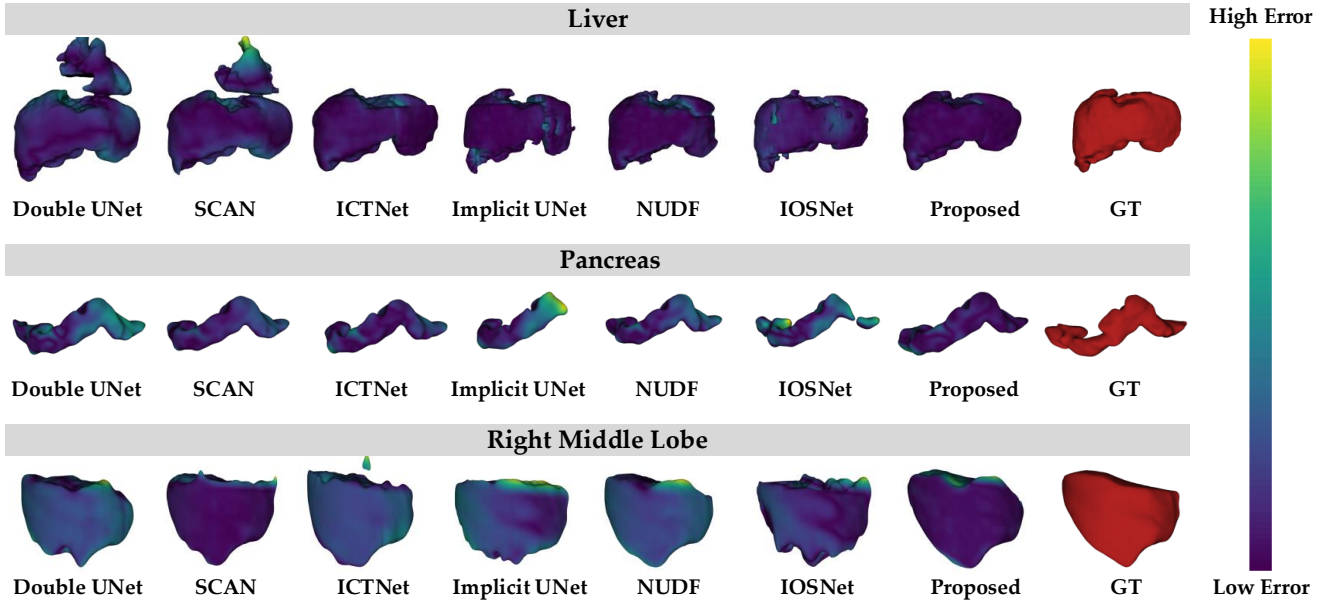


Fig. 6. Qualitative comparisons of shape modeling among the proposed methods with others. The dark purple indicates low reconstruction error, while bright yellow denotes high reconstruction error. Compared with other methods, our approach achieved more accurate refinement results.

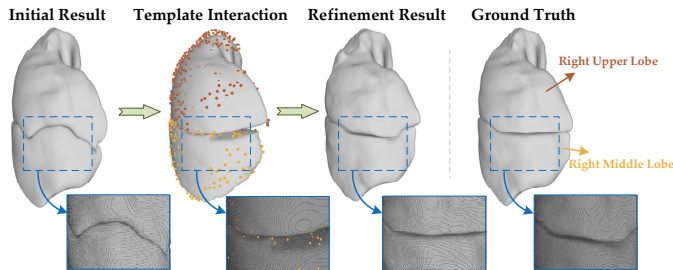


Fig. 7. Visualization of the multi lobes' refinement process via template interaction and implicit shape modeling. The example shows the interaction of the right upper lobe and the right middle lobe. the misclassification problem happens in the initial results. The template encodes each shape prior to the interaction, the refinement result demonstrates the improvement that they are closer to their independent ground-truth.

ments of CD and EMD. It is observed that our approach performed the best on shape modeling of different datasets, achieving average 0.232 CD / 0.087 EMD on Liver shape, 0.128 CD / 0.069 EMD on Pancreas shape, and 0.417 CD / 0.100 EMD on Lung Lobe shapes. Compared with the voxel-wise refinement methods(Araújo et al., 2019; Jha et al., 2020; Dai et al., 2018), they were limited in the discrete voxel representation, and the plausible structural prior knowledge is hard to acquire for refinement. The qualitative result, seen in Fig.6, also verified that these methods were hard to correct structural errors, e.g., Double UNet(Jha et al., 2020) and SCAN(Dai et al., 2018) generated anatomical error in Liver instances. As for the recent implicit-based segmentation methods(Marimont and Tarroni, 2022; Sørensen et al., 2022; Khan and Fang, 2022), our method performed better than theirs from two aspects. For one thing, they merely added the coordinate-based latent constraint in the segmentation process of CNNs, which does not

particularly break the limitation of the discrete voxel grid. We designed PICCT to align shapes to the canonical frame and then conducted the implicit shape modeling in the continuous space. For another, our model took the consideration that common structural prior knowledge should be shared across the same category of medical shapes. Fig.6 corroborated that the proposed method achieve superior accuracy of shape modeling than(Marimont and Tarroni, 2022; Sørensen et al., 2022; Khan and Fang, 2022).

With regard to the refinement procedure of multi lobes, Table 2 reported the quantitative results. The proposed method could decrease CD/EMD of each lobe to alleviate the misclassification problem. This can be credited to the independent template interaction and implicit refinement. As seen in Fig.7, we provided the refinement example of the right upper lobe and right middle lobe. It was observed that misclassification happened in the initial results, however, the learned template for each lobe is reasonable to interaction. The template encodes each shape prior for the interaction, and the right upper lobe and right middle lobe had been rectified according to their independent templates. As demonstrated in Fig.5 and Fig.7, the learned templates via deep INRs conforms to the anatomical shape priors, hence the following refinement procedure shares more explainability.

As mentioned before, we could conduct the inverse transform of PICCT of each instance to map the refinement shape surface to the volume result in the discrete space. Compared with the initial results generated by 3D UNet, the proposed implicit shape modeling refined the HD95 from 18.05 mm to 11.40 mm on the Liver dataset, from 4.91 mm to 4.13 mm on the Pancreas dataset, and from 14.97 mm to 12.04 mm on the Lung Lobe dataset. Table 3 demonstrated that the proposed method also performed better than other comparative methods, especially the surface distance based measurements HD95 and ASSD had

Table 3. Quantitative comparison of the Liver, Pancreas, and Lung Lobe datasets in the voxel-wise metric space.

Liver Dataset				
Method	DSC (%) \uparrow	NSD (%) \uparrow	HD95 (mm) \downarrow	ASSD (mm) \downarrow
Double-UNet (Jha et al., 2020)	82.40 \pm 17.58	70.77 \pm 16.83	81.06 \pm 61.51	16.42 \pm 38.47
SCAN (Dai et al., 2018)	86.68 \pm 5.94	74.02 \pm 10.23	60.05 \pm 35.92	7.19 \pm 4.23
ICTNet (Araújo et al., 2019)	87.78 \pm 6.45	71.61 \pm 10.23	38.30 \pm 28.50	5.54 \pm 3.62
Implicit U-Net (Marimont and Tarroni, 2022)	91.13 \pm 5.09	74.03 \pm 12.9	22.66 \pm 10.58	3.25 \pm 1.59
NUDF (Sørensen et al., 2022)	93.39 \pm 5.49	85.47 \pm 12.0	17.20 \pm 19.22	2.41 \pm 2.14
IOSNet (Khan and Fang, 2022)	86.48 \pm 6.52	61.98 \pm 14.67	49.11 \pm 34.31	7.13 \pm 4.70
Proposed	93.86 \pm 3.25	90.74 \pm 8.00	11.40 \pm 10.31	2.09 \pm 1.28
Pancreas Dataset				
Method	DSC (%) \uparrow	NSD (%) \uparrow	HD95 (mm) \downarrow	ASSD (mm) \downarrow
Double-UNet (Jha et al., 2020)	79.40 \pm 11.19	87.47 \pm 12.64	13.23 \pm 22.52	2.31 \pm 3.70
SCAN (Dai et al., 2018)	81.90 \pm 6.29	90.24 \pm 6.69	5.64 \pm 3.57	1.20 \pm 0.57
ICTNet (Araújo et al., 2019)	79.54 \pm 7.26	88.18 \pm 9.21	7.95 \pm 10.30	1.55 \pm 1.32
Implicit U-Net (Marimont and Tarroni, 2022)	68.47 \pm 11.30	77.31 \pm 13.28	19.08 \pm 19.61	3.26 \pm 3.46
NUDF (Sørensen et al., 2022)	82.14 \pm 5.17	90.46 \pm 5.14	6.44 \pm 5.73	1.26 \pm 0.45
IOSNet (Khan and Fang, 2022)	73.12 \pm 13.72	84.40 \pm 14.40	10.08 \pm 17.00	2.27 \pm 3.36
Proposed	83.18 \pm 5.89	92.21 \pm 5.13	4.13 \pm 2.18	1.09 \pm 0.38
Lung Lobe Dataset				
Method	DSC (%) \uparrow	NSD (%) \uparrow	HD95 (mm) \downarrow	ASSD (mm) \downarrow
Double-UNet (Jha et al., 2020)	92.55 \pm 7.00	82.71 \pm 12.65	15.97 \pm 14.79	2.20 \pm 2.04
SCAN (Dai et al., 2018)	92.52 \pm 7.00	83.53 \pm 10.28	15.78 \pm 12.68	2.10 \pm 1.63
ICTNet (Araújo et al., 2019)	92.59 \pm 8.00	83.81 \pm 11.29	16.36 \pm 16.42	2.20 \pm 2.08
Implicit U-Net (Marimont and Tarroni, 2022)	89.59 \pm 14.00	79.70 \pm 16.39	18.43 \pm 16.27	2.95 \pm 3.44
NUDF (Sørensen et al., 2022)	93.12 \pm 7.00	84.82 \pm 10.65	19.76 \pm 19.23	2.38 \pm 2.30
IOSNet (Khan and Fang, 2022)	87.06 \pm 16.00	73.43 \pm 17.07	21.59 \pm 15.17	3.93 \pm 4.31
Proposed	93.52 \pm 3.96	86.02 \pm 5.76	12.04 \pm 8.45	1.80 \pm 0.95

been improved substantially. Fig.8 provided the slices view of the comparison between the initial results and implicit refinement results. It can be observed that the under/over segment problem had been alleviated with the integration of template anatomical prior. In addition, the implicit refinement was performed in the continuous space, hence, the response near the boundary became more consistent, manifested as smoother.

5. Discussion

5.1. Ablation Study

Effectiveness of α and β : To valid the effect of components, α , and β , we conducted the ablation study in Table 4. Without instance code α , the CD/EMD suffered a performance decline. CD/EMD got worse results to 0.264/0.092 in the Liver dataset, 0.133/0.071 in the Pancreas dataset, and 0.485/0.103 in the

Table 4. Ablation study of the instance latent code α and hyper latent code β on Liver, Pancreas, and Lung Lobe datasets. Mean CD and EMD are reported.

Instance code α	Hyper code β	Liver		Pancreas		Lung Lobe	
		CD \downarrow	EMD \downarrow	CD \downarrow	EMD \downarrow	CD \downarrow	EMD \downarrow
\times	\times	0.342	0.104	0.188	0.089	0.621	0.112
\checkmark	\times	0.264	0.092	0.133	0.071	0.485	0.103
\times	\checkmark	0.275	0.095	0.137	0.074	0.512	0.108
\checkmark	\checkmark	0.232	0.087	0.128	0.069	0.417	0.100

Lobe dataset. It demonstrated the necessity to assign a unique latent code for each instance. Similarly, Without Hyper code β , the CD/EMD also encountered the degradation in CD/EMD to 0.275/0.095 in the Liver dataset, 0.137/0.074 in the Pancreas dataset, and 0.512/0.108 in the Lobe dataset. The β that forms

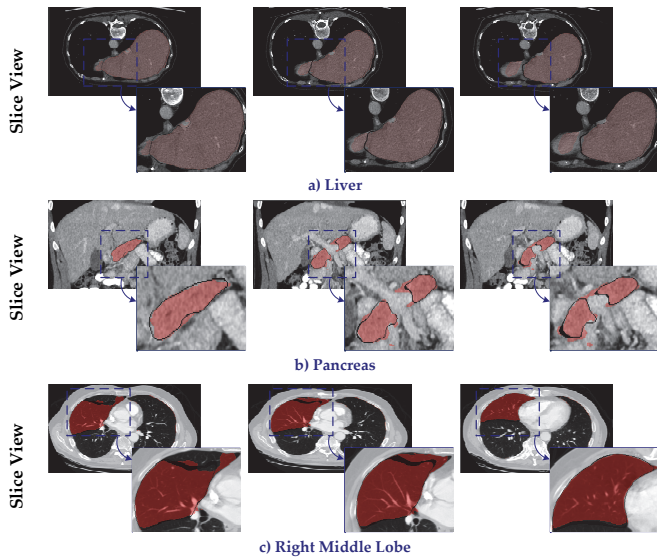


Fig. 8. Volume space comparison, results are shown in stacks of slices. The black contours denote the boundary results obtained from implicit refinement. Initial prediction results are labeled in red.

Table 5. Quantitative continuous metric space results of adding the proposed implicit refinement method to the nnUNet backbone on Liver, Pancreas, and Lung Lobe datasets.

Liver Dataset				
Method	CD (mean. \pm std.) \downarrow	EMD (mean. \pm std.) \downarrow	CD (median) \downarrow	EMD (median) \downarrow
nnUNet	0.128 \pm 0.118	0.089 \pm 0.024	0.078	0.089
nnUNet + Proposed	0.079 \pm 0.068	0.059 \pm 0.016	0.058	0.052
Pancreas Dataset				
Method	CD (mean. \pm std.) \downarrow	EMD (mean. \pm std.) \downarrow	CD (median) \downarrow	EMD (median) \downarrow
nnUNet	0.348 \pm 0.426	0.111 \pm 0.016	0.143	0.108
nnUNet + Proposed	0.155 \pm 0.002	0.082 \pm 0.015	0.077	0.079
Lung Lobe Dataset				
Method	CD (mean. \pm std.) \downarrow	EMD (mean. \pm std.) \downarrow	CD (median) \downarrow	EMD (median) \downarrow
nnUNet	0.361 \pm 0.520	0.105 \pm 0.023	0.163	0.101
nnUNet + Proposed	0.187 \pm 0.238	0.088 \pm 0.017	0.121	0.085

the hyper-network is helpful to encourage the weights of the deformation field to be instance-specific and better fuse the instance latent codes and corresponding coordinates.

Effectiveness of Regularization Constraints: To investigate the role of the regularization constraints, we performed the ablation study of $Deform_{\mathcal{H}(\beta)}$ and $Temp$. Fig.9 visualized the experimental results. For one thing, without the regularization of $Deform_{\mathcal{H}(\beta)}$, i.e., \mathcal{L}_{vec} and \mathcal{L}_{dis} , the instance-specific shape modeling achieved satisfactory results. However, the loose restriction on $Deform_{\mathcal{H}(\beta)}$ leads to the invalid template shape, as illustrated in the second row of Fig.9, which is detrimental to the subsequent template interaction and implicit refinement process. For another, the lack of regularization of $Temp$, i.e., \mathcal{L}_{tpn} , caused less accurate shape modeling of the instances and the sharable template structure cannot be extracted with high fidelity across the instances within the same category. In summary, $Deform_{\mathcal{H}(\beta)}$ and $Temp$ are two indispensable regularization constraints to guarantee the accurate implicit shape modeling with template generation.

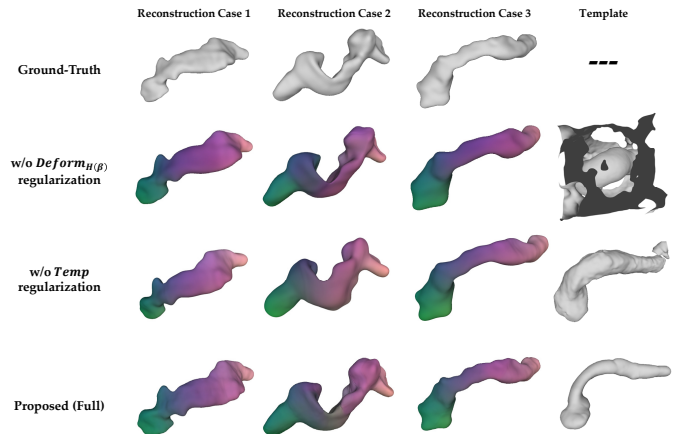


Fig. 9. Effect of the regularization constraints of the $Deform_{\mathcal{H}(\beta)}$ and $Temp$ on the Pancreas dataset.

Plug & Play Usage: We also demonstrated that the proposed implicit shape modeling of volumetric data shares the plug-and-play property. We embedded the implicit shape modeling to refine the initial results generated by the nnUNet (Isensee et al., 2021). nnUNet is a strong tool for medical image segmentation, however, it still lacks the shape prior knowledge during the optimization process. Table 5 revealed that the implicit refinement can further improve the initial results of nnUNet.

5.2. More Challenges and Future

One of the promising applications of the proposed method is to refine the imperfect annotation of volumetric data, which can substantially relieve the burden of precise labeling. It is feasible because the class-wise template shape prior has been learned in the continuous space across all collected instances. Further, this template shape prior could bring guidance into the imperfect annotation of unseen data to perform the implicit refinement. In addition, shape registration can be performed based on the implicit neural fields. Each instance is wrapped to the template space via an implicit deformation field. Hence, the dense correspondences between instances could be built through the connection of the implicit template. The implicit shape modeling with template registration provides the registered 3D shapes, which can be further transformed into virtual anatomical models. These virtual models are beneficial to the AR-based anatomy education (Bölek et al., 2021).

Our work focused on the implicit shape modeling of the medical organs that share common structures within the same category. However, affected by the diseases or surgeries, the anatomical structure of organs can be changed for patients, for example, the hepatic segmentectomy would change the original liver shape. The current learned implicit template cannot be well generalized to specific cases with non-existent partial structures. One potential future solution is to extend the implicit representation to jointly learn a global shape prior with local anatomical-varying structures conditioned by the image intensity distribution. In addition, the current approach generates independent implicit templates for multi-class medical shapes. To model the multi-class shapes in a unified implicit

neural network is challenging. For example, the lobes interact with each other closely, leading to the accurate SDF values are difficult to acquire since the fissure interface is hardly visible from any camera view. Hence, to compensate for SDF values, other supervision signals should be further explored to characterize the representation of the implicit field.

6. Conclusion

In this paper, we proposed a unified implicit neural field framework for the refinement of medical image segmentation. To learn an explainable shape prior across instances within the category, the PICCT first transforms the input volumetric data to an aligned manner in the continuous space, and then be fed into the INRs. Further, we introduce implicit surface physical constraints on top of the signed distance function (SDF) into the implicit shape modeling of both instances and latent template to better learn shape representation and correspondence. For the inference phase, TIM refines initial results by deforming the implicit template with instance-specific latent codes. Experimental results on three datasets demonstrated the superiority of our approach in shape refinement compared with other state-of-the-art methods.

Author contributions

M.Z: Conceptualization, Methodology, Software, Validation, Formal analysis, Writing- original draft; **H.Z:** Conceptualization, Writing- review and editing; **X.Y:** Conceptualization, Writing- review and editing; **G.Z.Y:** Conceptualization, Critical Evaluation, Supervision, Writing- review and editing; **Y.G:** Conceptualization, Methodology, Critical Evaluation, Supervision, Writing- review and editing.

Declaration of Competing Interest

The authors declare that they have no known competing financial interests or personal relationships that could be appeared to influence the work reported in this paper.

Acknowledgements

This work is supported in part by NSFC under Grant 62373243, and in part by Shanghai Municipal of Science and Technology Project, under Grant 20JC1419500 and Grant 20DZ2220400.

References

Antonelli, M., Reinke, A., Bakas, S., Farahani, K., Kopp-Schneider, A., Landman, B.A., Litjens, G., Menze, B., Ronneberger, O., Summers, R.M., et al., 2022. The medical segmentation decathlon. *Nature communications* 13, 4128.

Araújo, R.J., Cardoso, J.S., Oliveira, H.P., 2019. A deep learning design for improving topology coherence in blood vessel segmentation, in: *Medical Image Computing and Computer Assisted Intervention–MICCAI 2019: 22nd International Conference, Shenzhen, China, October 13–17, 2019, Proceedings, Part I 22*, Springer. pp. 93–101.

Bishop, C.M., 1995. *Neural networks for pattern recognition*. Oxford university press.

Bölek, K.A., De Jong, G., Henssen, D., 2021. The effectiveness of the use of augmented reality in anatomy education: a systematic review and meta-analysis. *Scientific Reports* 11, 15292.

Carr, J.C., Beatson, R.K., Cherrie, J.B., Mitchell, T.J., Fright, W.R., McCallum, B.C., Evans, T.R., 2001. Reconstruction and representation of 3d objects with radial basis functions, in: *Proceedings of the 28th annual conference on Computer graphics and interactive techniques*, pp. 67–76.

Chabra, R., Lenssen, J.E., Ilg, E., Schmidt, T., Straub, J., Lovegrove, S., Newcombe, R., 2020. Deep local shapes: Learning local sdf priors for detailed 3d reconstruction, in: *Computer Vision–ECCV 2020: 16th European Conference, Glasgow, UK, August 23–28, 2020, Proceedings, Part XXIX 16*, Springer. pp. 608–625.

Chang, A.X., Funkhouser, T., Guibas, L., Hanrahan, P., Huang, Q., Li, Z., Savarese, S., Savva, M., Song, S., Su, H., et al., 2015. Shapenet: An information-rich 3d model repository. *arXiv preprint arXiv:1512.03012*.

Chen, Z., Zhang, H., 2019. Learning implicit fields for generative shape modeling, in: *Proceedings of the IEEE/CVF Conference on Computer Vision and Pattern Recognition*, pp. 5939–5948.

Chibane, J., Alldieck, T., Pons-Moll, G., 2020. Implicit functions in feature space for 3d shape reconstruction and completion, in: *Proceedings of the IEEE/CVF conference on computer vision and pattern recognition*, pp. 6970–6981.

Çiçek, Ö., Abdulkadir, A., Lienkamp, S.S., Brox, T., Ronneberger, O., 2016. 3d u-net: learning dense volumetric segmentation from sparse annotation, in: *Medical Image Computing and Computer-Assisted Intervention–MICCAI 2016: 19th International Conference, Athens, Greece, October 17–21, 2016, Proceedings, Part II 19*, Springer. pp. 424–432.

Cootes, T.F., Taylor, C.J., Cooper, D.H., Graham, J., 1992. Training models of shape from sets of examples, in: *BMVC92: Proceedings of the British Machine Vision Conference, organised by the British Machine Vision Association 22–24 September 1992 Leeds*, Springer. pp. 9–18.

Cremers, D., Rousson, M., Deriche, R., 2007. A review of statistical approaches to level set segmentation: integrating color, texture, motion and shape. *International journal of computer vision* 72, 195–215.

Dai, W., Dong, N., Wang, Z., Liang, X., Zhang, H., Xing, E.P., 2018. Scan: Structure correcting adversarial network for organ segmentation in chest x-rays, in: *Deep Learning in Medical Image Analysis and Multimodal Learning for Clinical Decision Support: 4th International Workshop, DLMIA 2018, and 8th International Workshop, ML-CDS 2018, Held in Conjunction with MICCAI 2018, Granada, Spain, September 20, 2018, Proceedings 4*, Springer. pp. 263–273.

David, H., Andrew, M.D., Quoc, V.L., 2017. Hypernetworks, in: *Proceedings of International Conference on Learning Representations*.

Dempster, A.P., Laird, N.M., Rubin, D.B., 1977. Maximum likelihood from incomplete data via the em algorithm. *Journal of the royal statistical society: series B (methodological)* 39, 1–22.

Deng, Y., Yang, J., Tong, X., 2021. Deformed implicit field: Modeling 3d shapes with learned dense correspondence, in: *Proceedings of the IEEE/CVF Conference on Computer Vision and Pattern Recognition*, pp. 10286–10296.

Dou, Q., Yu, L., Chen, H., Jin, Y., Yang, X., Qin, J., Heng, P.A., 2017. 3d deeply supervised network for automated segmentation of volumetric medical images. *Medical image analysis* 41, 40–54.

Edgcombe, P., Pratt, P., Yang, G.Z., Nguan, C., Rohling, R., 2015. Pico lantern: Surface reconstruction and augmented reality in laparoscopic surgery using a pick-up laser projector. *Medical image analysis* 25, 95–102.

Fan, H., Su, H., Guibas, L.J., 2017. A point set generation network for 3d object reconstruction from a single image, in: *Proceedings of the IEEE conference on computer vision and pattern recognition*, pp. 605–613.

Gropp, A., Yariv, L., Haim, N., Atzmon, M., Lipman, Y., 2020. Implicit geometric regularization for learning shapes. *arXiv preprint arXiv:2002.10099*.

Gunning, D., Stefik, M., Choi, J., Miller, T., Stumpf, S., Yang, G.Z., 2019. Xai—explainable artificial intelligence. *Science robotics* 4, eaay7120.

He, K., Zhang, X., Ren, S., Sun, J., 2015. Delving deep into rectifiers: Surpassing human-level performance on imagenet classification, in: *Proceedings of the IEEE international conference on computer vision*, pp. 1026–1034.

Heimann, T., Meinzer, H.P., 2009. Statistical shape models for 3d medical image segmentation: a review. *Medical image analysis* 13, 543–563.

Huber, T., Paschold, M., Hansen, C., Wunderling, T., Lang, H., Kneist, W.,

2017. New dimensions in surgical training: immersive virtual reality laparoscopic simulation exhilarates surgical staff. *Surgical endoscopy* 31, 4472–4477.
- Iglesias, J.E., Sabuncu, M.R., 2015. Multi-atlas segmentation of biomedical images: a survey. *Medical image analysis* 24, 205–219.
- Isensee, F., Jaeger, P.F., Kohl, S.A., Petersen, J., Maier-Hein, K.H., 2021. nnu-net: a self-configuring method for deep learning-based biomedical image segmentation. *Nature methods* 18, 203–211.
- Isola, P., Zhu, J.Y., Zhou, T., Efros, A.A., 2017. Image-to-image translation with conditional adversarial networks, in: *Proceedings of the IEEE conference on computer vision and pattern recognition*, pp. 1125–1134.
- Jha, D., Riegler, M.A., Johansen, D., Halvorsen, P., Johansen, H.D., 2020. Doubleu-net: A deep convolutional neural network for medical image segmentation, in: *2020 IEEE 33rd International symposium on computer-based medical systems (CBMS)*, IEEE. pp. 558–564.
- Jiang, C., Sud, A., Makadia, A., Huang, J., Nießner, M., Funkhouser, T., et al., 2020. Local implicit grid representations for 3d scenes, in: *Proceedings of the IEEE/CVF Conference on Computer Vision and Pattern Recognition*, pp. 6001–6010.
- Khan, M.O., Fang, Y., 2022. Implicit neural representations for medical imaging segmentation, in: *Medical Image Computing and Computer Assisted Intervention–MICCAI 2022: 25th International Conference, Singapore, September 18–22, 2022, Proceedings, Part V*, Springer. pp. 433–443.
- Kingma, D.P., Ba, J., 2014. Adam: A method for stochastic optimization. *arXiv preprint arXiv:1412.6980*.
- Kingma, D.P., Welling, M., 2014. Auto-encoding variational bayes .
- Krass, S., Lassen-Schmidt, B., Schenk, A., 2022. Computer-assisted image-based risk analysis and planning in lung surgery—a review. *Frontiers in Surgery* 9, 920457.
- Litjens, G., Kooi, T., Bejnordi, B.E., Setio, A.A.A., Ciampi, F., Ghafoorian, M., Van Der Laak, J.A., Van Ginneken, B., Sánchez, C.I., 2017. A survey on deep learning in medical image analysis. *Medical image analysis* 42, 60–88.
- Lorensen, W.E., Cline, H.E., 1998. Marching cubes: A high resolution 3d surface construction algorithm, in: *Seminal graphics: pioneering efforts that shaped the field*, pp. 347–353.
- Marimont, S.N., Tarroni, G., 2022. Implicit u-net for volumetric medical image segmentation, in: *Annual Conference on Medical Image Understanding and Analysis*, Springer. pp. 387–397.
- Mescheder, L., Oechsle, M., Niemeyer, M., Nowozin, S., Geiger, A., 2019. Occupancy networks: Learning 3d reconstruction in function space, in: *Proceedings of the IEEE/CVF conference on computer vision and pattern recognition*, pp. 4460–4470.
- Myronenko, A., Song, X., 2009. On the closed-form solution of the rotation matrix arising in computer vision problems. *arXiv preprint arXiv:0904.1613*.
- Myronenko, A., Song, X., 2010. Point set registration: Coherent point drift. *IEEE transactions on pattern analysis and machine intelligence* 32, 2262–2275.
- Nikolov, S., Blackwell, S., Zverovitch, A., Mendes, R., Livne, M., De Fauw, J., Patel, Y., Meyer, C., Askham, H., Romera-Paredes, B., et al., 2018. Deep learning to achieve clinically applicable segmentation of head and neck anatomy for radiotherapy. *arXiv preprint arXiv:1809.04430*.
- Osher, S., Fedkiw, R., Piechor, K., 2004. Level set methods and dynamic implicit surfaces. *Appl. Mech. Rev.* 57, B15–B15.
- Park, J.J., Florence, P., Straub, J., Newcombe, R., Lovegrove, S., 2019. Deepsdf: Learning continuous signed distance functions for shape representation, in: *Proceedings of the IEEE/CVF conference on computer vision and pattern recognition*, pp. 165–174.
- Pelani, E., Kumar, R.P., Aghayan, D.L., Palomar, R., Fretland, Å.A., Brun, H., Elle, O.J., Edwin, B., 2020. Use of mixed reality for improved spatial understanding of liver anatomy. *Minimally Invasive Therapy & Allied Technologies* 29, 154–160.
- Peng, S., Niemeyer, M., Mescheder, L., Pollefeys, M., Geiger, A., 2020. Convolutional occupancy networks, in: *Computer Vision–ECCV 2020: 16th European Conference, Glasgow, UK, August 23–28, 2020, Proceedings, Part III* 16, Springer. pp. 523–540.
- Preuss, K., Thach, N., Liang, X., Baine, M., Chen, J., Zhang, C., Du, H., Yu, H., Lin, C., Hollingsworth, M.A., et al., 2022. Using quantitative imaging for personalized medicine in pancreatic cancer: a review of radiomics and deep learning applications. *Cancers* 14, 1654.
- Ramalhinho, J., Yoo, S., Dowrick, T., Koo, B., Somasundaram, M., Gurusamy, K., Hawkes, D.J., Davidson, B., Blandford, A., Clarkson, M.J., 2023. The value of augmented reality in surgery—a usability study on laparoscopic liver surgery. *Medical Image Analysis* 90, 102943.
- Ronneberger, O., Fischer, P., Brox, T., 2015. U-net: Convolutional networks for biomedical image segmentation, in: *Medical Image Computing and Computer-Assisted Intervention–MICCAI 2015: 18th International Conference, Munich, Germany, October 5–9, 2015, Proceedings, Part III* 18, Springer. pp. 234–241.
- Roth, H.R., Lu, L., Farag, A., Shin, H.C., Liu, J., Turkbey, E.B., Summers, R.M., 2015. Deeporgan: Multi-level deep convolutional networks for automated pancreas segmentation, in: *Medical Image Computing and Computer-Assisted Intervention–MICCAI 2015: 18th International Conference, Munich, Germany, October 5–9, 2015, Proceedings, Part I* 18, Springer. pp. 556–564.
- Rubner, Y., Tomasi, C., Guibas, L.J., 1998. A metric for distributions with applications to image databases, in: *Sixth international conference on computer vision (IEEE Cat. No. 98CH36271)*, IEEE. pp. 59–66.
- Shen, C., O’Brien, J.F., Shewchuk, J.R., 2004. Interpolating and approximating implicit surfaces from polygon soup, in: *ACM SIGGRAPH 2004 Papers*, pp. 896–904.
- Sitzmann, V., Martel, J., Bergman, A., Lindell, D., Wetzstein, G., 2020. Implicit neural representations with periodic activation functions. *Advances in neural information processing systems* 33, 7462–7473.
- Sitzmann, V., Zollhöfer, M., Wetzstein, G., 2019. Scene representation networks: Continuous 3d-structure-aware neural scene representations. *Advances in Neural Information Processing Systems* 32.
- Sørensen, K., Camara, O., De Backer, O., Kofoed, K.F., Paulsen, R.R., 2022. Nudf: Neural unsigned distance fields for high resolution 3d medical image segmentation, in: *2022 IEEE 19th International Symposium on Biomedical Imaging (ISBI)*, IEEE. pp. 1–5.
- Tajbakhsh, N., Jeyaseelan, L., Li, Q., Chiang, J.N., Wu, Z., Ding, X., 2020. Embracing imperfect datasets: A review of deep learning solutions for medical image segmentation. *Medical Image Analysis* 63, 101693.
- Tang, H., Zhang, C., Xie, X., 2019. Automatic pulmonary lobe segmentation using deep learning, in: *2019 IEEE 16th international symposium on biomedical imaging (ISBI 2019)*, IEEE. pp. 1225–1228.
- Wang, H., Suh, J.W., Das, S.R., Pluta, J.B., Craige, C., Yushkevich, P.A., 2012. Multi-atlas segmentation with joint label fusion. *IEEE transactions on pattern analysis and machine intelligence* 35, 611–623.
- Willaert, W.I., Aggarwal, R., Van Herzele, I., Cheshire, N.J., Vermassen, F.E., 2012. Recent advancements in medical simulation: patient-specific virtual reality simulation. *World journal of surgery* 36, 1703–1712.
- Xu, Q., Wang, W., Ceylan, D., Mech, R., Neumann, U., 2019. Disn: Deep implicit surface network for high-quality single-view 3d reconstruction. *Advances in neural information processing systems* 32.
- Zheng, Z., Yu, T., Dai, Q., Liu, Y., 2021. Deep implicit templates for 3d shape representation, in: *Proceedings of the IEEE/CVF Conference on Computer Vision and Pattern Recognition*, pp. 1429–1439.
- Zhou, S.K., Greenspan, H., Davatzikos, C., Duncan, J.S., Van Ginneken, B., Madabhushi, A., Prince, J.L., Rueckert, D., Summers, R.M., 2021. A review of deep learning in medical imaging: Imaging traits, technology trends, case studies with progress highlights, and future promises. *Proceedings of the IEEE* 109, 820–838.